

1 **Swelling of Transported Smoke from Savanna fires over the Southeast Atlantic Ocean**

2 J. Kar^{1,2}, M. Vaughan², J. Tackett^{1,2}, Z. Liu², A. Omar², S. Rodier^{1,2}, C. Trepte², P. Lucker^{1,2}

3 ¹ Science Systems and Applications Inc., Hampton, VA

4 ² NASA Langley Research Center, Hampton, VA

5
6 **Corresponding author:** J. Kar, Science Systems and Applications Inc. (SSAI), NASA LaRC,
7 Hampton, Va 23681, USA. E-mail: jayanta.kar@nasa.gov

8
9 **Abstract.**

10 We use the recently released Cloud Aerosol Lidar and Infrared Pathfinder Satellite Observations
11 (CALIPSO) Version 4.1 (V4) lidar data to study the smoke plumes transported from Southern
12 African biomass burning areas. Significant improvements in the CALIPSO V4 Level 1 calibration
13 and V4 Level 2 algorithms lead to a better representation of their optical properties, with the
14 aerosol subtype improvements being particularly relevant to smoke over this area. For the first
15 time, we show evidence of smoke particles increasing in size, as demonstrated by their particulate
16 color ratios, as they are transported over the South Atlantic Ocean from the source regions over
17 Southern Africa. We hypothesize that this is due to hygroscopic swelling of the smoke particles
18 and is reflected in the higher relative humidity in the middle troposphere for profiles with smoke.
19 This finding may have implications for radiative forcing estimates over this area and is also
20 relevant to the ORACLES field mission.

21 **Keywords:** CALIPSO lidar measurements, African smoke, Evolution of optical properties

22 **1. Introduction:**

23 The impact of different types of aerosols on our environment is not very well understood and there
24 is an ever-increasing need to characterize the various aerosol types in different parts of the globe
25 (IPCC, 2013). In particular, the smoke from biomass burning needs to be better understood
26 because of the important radiative effects of black carbon (Bond et al., 2013), and because forest
27 fires have been growing in size and frequency in many parts of the world. As such, there have been
28 many studies of smoke from biomass burning, its properties and their evolution with time (e.g.,
29 Reid et al., 2005; Semeniuk et al., 2007; Saide et al., 2015). Some of these properties depend upon
30 the location and type of burning (e.g., smoldering or flaming).

31 Over Southern Africa, savanna burning occurs every year between June and October and
32 constitutes the largest source of biomass burning smoke over the globe (Van der Werf et al., 2010;
33 IPCC, 2013). The smoke plumes from these fires are transported over the Southeast Atlantic Ocean
34 within 5-7 days, overlying one of the largest low altitude extended stratus cloud decks anywhere
35 on the globe, which has consequences for radiative forcing estimates in this area. The direct
36 radiative forcing can be complex under such circumstances, changing from cooling in absence of
37 clouds to potentially heating at the top of the atmosphere, depending upon the aerosol loading as
38 well as the albedo and fractional coverage of the underlying clouds (Chand et al., 2009; Wilcox,
39 2012; Yu and Zhang, 2013). Passive satellite sensors have generally limited utility here because
40 the aerosol retrievals are done mostly for cloud-free conditions. However, progress has been made
41 in recent years, with researchers exploiting the spectral dependence of the absorption of the
42 upwelling radiation by the aerosols to simultaneously retrieve the cloud and aerosol optical depths
43 for cloudy scenes (Jethva et al., 2013, 2016; Meyer et al., 2015; Sayer et al., 2016). Multi-angle
44 polarization information from the POLDER instrument has also been utilized to retrieve the AOD

45 (Waquet et al., 2012; Peers et al. 2015; Deaconu et al., 2017). However, passive sensors cannot
46 provide vertically resolved information on these clouds and aerosols, which is crucial for a proper
47 assessment of the radiative forcing, both direct and indirect. This vertical information has become
48 possible in the last decade because of the space borne lidar CALIPSO, which has been providing
49 high quality measurements of the aerosol vertical profiles globally since June 2006 (Winker et al.,
50 2009). Measurements from CALIPSO have been used to derive accurate estimates of radiative
51 forcing of the aerosols above clouds in this region (Chand et al., 2008, 2009).

52 In the CALIPSO data processing sequence, the attenuated backscatter data are first
53 examined to detect layers using a thresholding algorithm (Vaughan et al., 2009) and then the layers
54 are classified as either a cloud or aerosol (Liu et al., 2009). The aerosol layers are subsequently
55 assigned various subtypes based on their optical properties (layer integrated attenuated backscatter
56 and estimated particulate depolarization ratio), the underlying surface type and altitude of the layer
57 (Omar et al., 2009). The November 2016 release of Version 4.1 (V4) of the CALIPSO lidar Level
58 2 data products incorporates significant improvements to the retrieval algorithms, including the
59 aerosol subtype assignments. These changes have improved the global characterization of aerosol
60 types using the CALIPSO measurements. In particular, there was a significant anomaly in the
61 subtyping over the Southeast Atlantic in earlier versions, where many smoke layers were
62 misclassified as marine layers. This has since been addressed in V4. Many more smoke layers are
63 now identified over the Atlantic, thus presenting a good opportunity for further study of these
64 extensive and regularly occurring smoke plumes. In particular, the evolution of the optical
65 properties of these smoke plumes as they are transported great distances over the South Atlantic
66 may now be better characterized.

67 In this short report, we use V4 CALIPSO data to present evidence of the evolution of size
68 of the smoke particles being exported from the Southern African savanna burning zones. We show
69 that these particles tend to increase in size as they are transported large distances over the ocean.
70 Recent work has noted a close correlation between the smoke plumes and moisture over the South
71 east Atlantic with a general increase in mid-tropospheric moisture in polluted conditions (Adebiyi
72 et al., 2015). While most constituents of smoke plumes are generally hydrophobic, aging and
73 oxidation processes during the transport might make them hydrophilic, and the signatures of this
74 behavior could be discerned in the relative humidity data. This result will have implications for
75 regional radiative forcing as well as for simulations of the transport of these extensive smoke
76 plumes and should be of interest to the currently ongoing ObseRvations of Aerosols above CLouds
77 and their intEractionS (ORACLES) aircraft mission studying the smoke and its interaction with
78 clouds over the same area (Zuidema et al., 2016).

79

80 **2. Data:**

81 We use the CALIPSO V4 level 2 aerosol profile product, which reports height-resolved profiles
82 of the total backscatter and extinction coefficients at 532 nm and 1064 nm, as well as the
83 perpendicular backscatter coefficients at 532 nm for all layers detected. The horizontal resolution
84 of the data is 5km while the vertical resolution is 60m up to 20km and 180m above that. As part
85 of the V4 level 2 updates, the retrieval algorithms were optimized to take maximum advantage of
86 the changes in the V4 level 1 data, released earlier, with significant improvements in both the 532
87 nm and 1064 nm channel calibrations (Getzewich et al., 2015). In particular, the improvement in
88 1064 nm channel calibration makes it feasible to study the optical properties of particles using both

89 the channels with a higher degree of confidence in this new data set. We shall use the particulate
90 color ratio (χ) of the aerosols, which is defined by the relation:

$$91 \quad \chi(z) = \frac{\beta_{1064}(z)}{\beta_{532}(z)} \quad (1)$$

92 where $\beta_{1064}(z)$ and $\beta_{532}(z)$ are the particulate backscatter coefficients retrieved at altitude z at
93 1064 nm and 532 nm, respectively. The particulate color ratio values derived from CALIPSO
94 measurements for the various subtypes typically range from 0 to 2, with the small particles like
95 smoke, polluted continental, clean and polluted dust generally having a broad peak near 0.5, while
96 coarse particles like dust, marine and dusty marine have a broad peak near 0.7 or so. The
97 uncertainties of the retrieved backscatter coefficients are somewhat larger for 1064 nm than 532
98 nm, and the estimated uncertainties for the particulate color ratios for the various subtypes
99 generally peak around 150% - 200%.

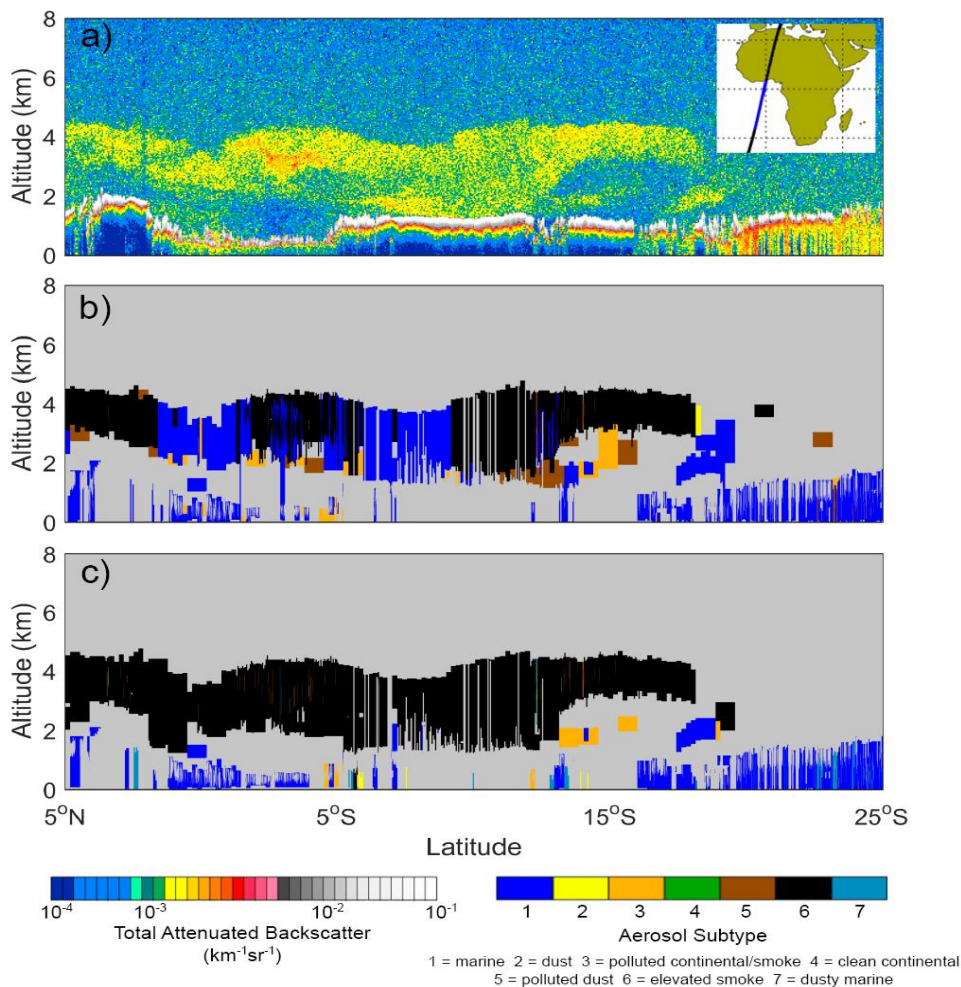
100 Within the troposphere, the primary modifications to aerosol subtypes in V4 are a) all
101 aerosol subtypes can now be identified within the polar regions; b) a new subtype called “dusty
102 marine” has been introduced to allow for mixing of transported dust with marine aerosols and c)
103 no distinction is made between polluted continental and smoke layers below the planetary
104 boundary layer, while the non-depolarizing elevated layers with layer tops above 2.5 km are now
105 classified as “elevated smoke”. We use aerosol layers that have been designated as either “polluted
106 continental/smoke” or “elevated smoke” by the CALIOP level 2 aerosol classification algorithm
107 for our analysis. Previous iterations of the CALIPSO aerosol subtype assignments have been
108 validated by comparison with AERONET data as well as High Spectral Resolution Lidar (HSRL)
109 data (Mielonen et al., 2009; Misra et al., 2013; Burton et al., 2013; Bibi et al., 2016). We also use
110 the 1064 nm measurements retrieved from the Cloud-Aerosol Transport System (CATS) lidar on

111 board the International Space Station (ISS) Mode 7.2 Version 2-01 Level 2 Operational (L2O)
 112 Layer and Profile data products. The CATS lidar measures 1064 nm elastic backscatter in
 113 polarization planes parallel and perpendicular to the transmitted linearly polarized laser pulses,
 114 thus providing depolarization ratio data at 1064 nm since March 2015 (Yorks et al., 2016).

115 3. Results

116 3.1. Particulate color ratio evolution in transported smoke.

117



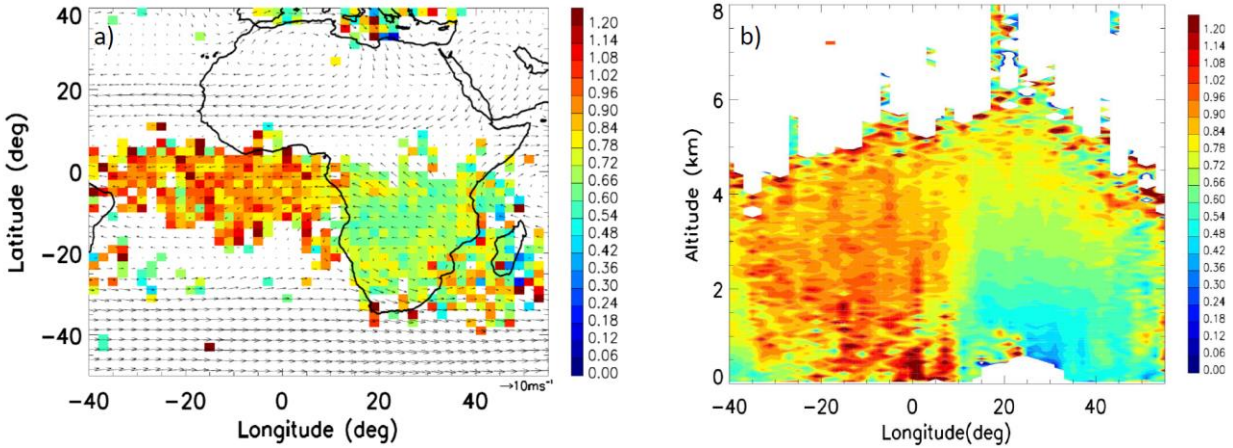
118

119 **Figure 1.** CALIPSO browse images from September 5, 2010 of a) 532 nm attenuated
120 backscatter coefficients; and b) aerosol subtypes reported in the V3 data products; and c)
121 aerosol subtypes reported in the V4 data products.

122 Figure 1a shows the nighttime 532 nm attenuated backscatter coefficients measured over the South
123 Atlantic Ocean off the coast of Southern Africa on September 5, 2010. The extended plume at 2-
124 5 km altitude between 19°S and 5°N is smoke that has been transported from the extensive fires
125 that occur over Southern Africa between June and October every year. Figure 1b shows the aerosol
126 subtypes assigned in the Version 3 (V3) data products. As can be seen, in the V3 analysis the
127 plume between 2 and 5 km is punctuated by a large number of misclassified marine layers (in
128 blue). The misclassification of smoke layers as marine was a pervasive problem in V3 data over
129 this area. Figure 1c shows the recently released V4 data, where now we can see a fuller and more
130 coherent smoke plume. With the improvements incorporated into the aerosol subtyping scheme,
131 the V4 analysis reports a much larger number of smoke layers (and an upward revision of the
132 aerosol optical depth) over this most important and extensive biomass burning area. Thus, we now
133 have more representative information about the spatial extent of biomass burning plumes in this
134 region so that we can better exploit the optical properties reported in the CALIPSO data products.

135

136



137

138

139

140

141

142

Figure 2. a) Particulate color ratio distribution of smoke at 3 km for August, 2006-2010, binned in increments of 2° latitude and 2° longitude, with wind vectors at 700 hPa from MERRA-2 (August 2006-2010) binned in increments of 2.5° latitude and 2.5° longitude; and b) height-longitude cross section of particulate color ratio along $0-25^\circ\text{S}$ (August 2006-2010). Only nighttime data are used.

143

144

145

146

147

148

149

150

151

152

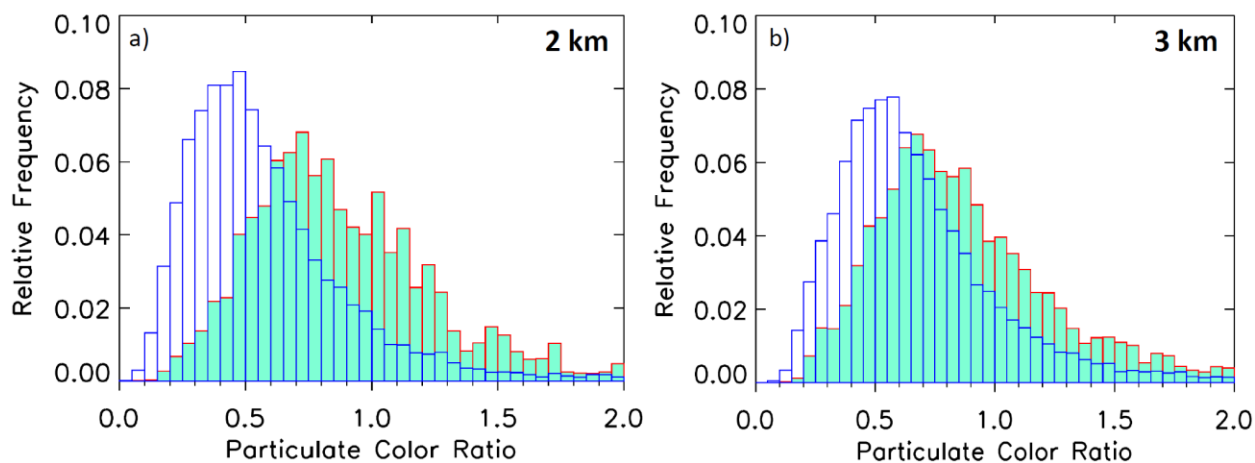
153

Figure 2a shows the spatial distribution of the particulate color ratio of the aerosol samples classified as smoke at 3 km using nighttime data for the month of August averaged over 2006-2010. As mentioned above, the particulate color ratio is the ratio of the total backscatter coefficients at 1064 nm and 532 nm, and provides a measure of aerosol particle size. The data shown in Figure 2 used only cloud free nighttime profiles. Further, we have included data from only those profiles which had the extinction quality control flag as either zero, indicating that the initial lidar ratio resulted in stable extinction retrievals, or one, which flags those cases where the lidar ratio could be inferred directly from the data. We also filtered out those data points where the extinction uncertainty estimate diverged and those where the uncertainty of particulate color ratio exceeds 500%. The uncertainty filters retain about 93% of the samples in the region between the equator and 35°S and 35°W - 55°E . A minimum number of 15 samples was required for each grid

154 box. As can be seen in Figure 2a, there is a clear increase in the particulate color ratio values from
155 the source areas over land to those over the ocean. This likely represents an increase in the size of
156 the smoke particles as they are swept over the ocean over 5-7 days. To our knowledge, this is the
157 first time that evidence for a potential increase in the size of the smoke particles derived from
158 satellite data is being reported over this area. The full altitude range of the data can be seen in
159 Figure 2b, which shows the height-longitude cross-section of the particulate color ratios over 0-
160 25°S, using only the cloud free nighttime profiles for August 2006-2010. Once again, the
161 difference between the land and ocean can be clearly seen with somewhat higher values at the
162 lowest altitudes over the ocean, which might be due to gravitational settling of relatively larger
163 and heavier particles.

164

165



166

167 **Figure 3.** Histograms of particulate color ratio over land (25°S-0,10°E-35°E, in blue) and
168 ocean (25°S-0, 30°W-10°E, in aquamarine, filled) at a) 2 km and b) 3 km (August 2006-
169 2010).

170 Figures 3a and 3b show the histograms of the particulate color ratio at 2 km and 3 km respectively
171 over the source regions on land (in blue, between 25°S-equator, 10°E-35°E) and over oceanic
172 regions (in aquamarine, filled, between 25°S-equator, 30°W-10°E) for August 2006-2010. There
173 is a significant difference in the color ratio distribution between land and ocean, with the
174 distribution significantly shifted toward higher values over the ocean at both altitudes, and a much
175 sharper difference at 2 km. At 3 km, the mean particulate color ratio over land is ~0.7 while that
176 over the ocean is ~0.9, an increase of ~29%, while the increase at 2 km is ~ 60%. This increase in
177 particulate color ratio for smoke particles was seen for all months between June and October and
178 in all years, with some interannual variability. Similar results were also obtained using the daytime
179 data, although the latter has significantly more noise than the nighttime (not shown). Given that
180 this phenomenon occurs consistently for the key biomass burning months every year, it is not likely
181 to be a data artifact.

182 Apart from the smoke that is transported to the Atlantic, there is another pathway that
183 transports smoke plumes from the southern Africa to the Indian Ocean. This has been noted in
184 satellite data (Swap et al., 1998) and has been known as the “river of smoke”. This outflow can be
185 seen in Figure 2 south of 20°S and between 30°E-55°E. While there is some suggestion of a similar
186 increased color ratio as compared to the land, there is more noise as compared to the outflow to
187 the southeast Atlantic. Further, the signature is not clearly seen in the spatial distribution at other
188 altitudes (not shown). Therefore we shall restrict our discussion to the transport to the southeast
189 Atlantic Ocean only.

190 The current version (V4.1) of the CALIPSO data processing scheme employs the Modern
191 Era Retrospective Analysis for Research and Applications version 2 (MERRA-2) for
192 meteorological information. The latter, for the first time, assimilates aerosol optical depth (AOD)

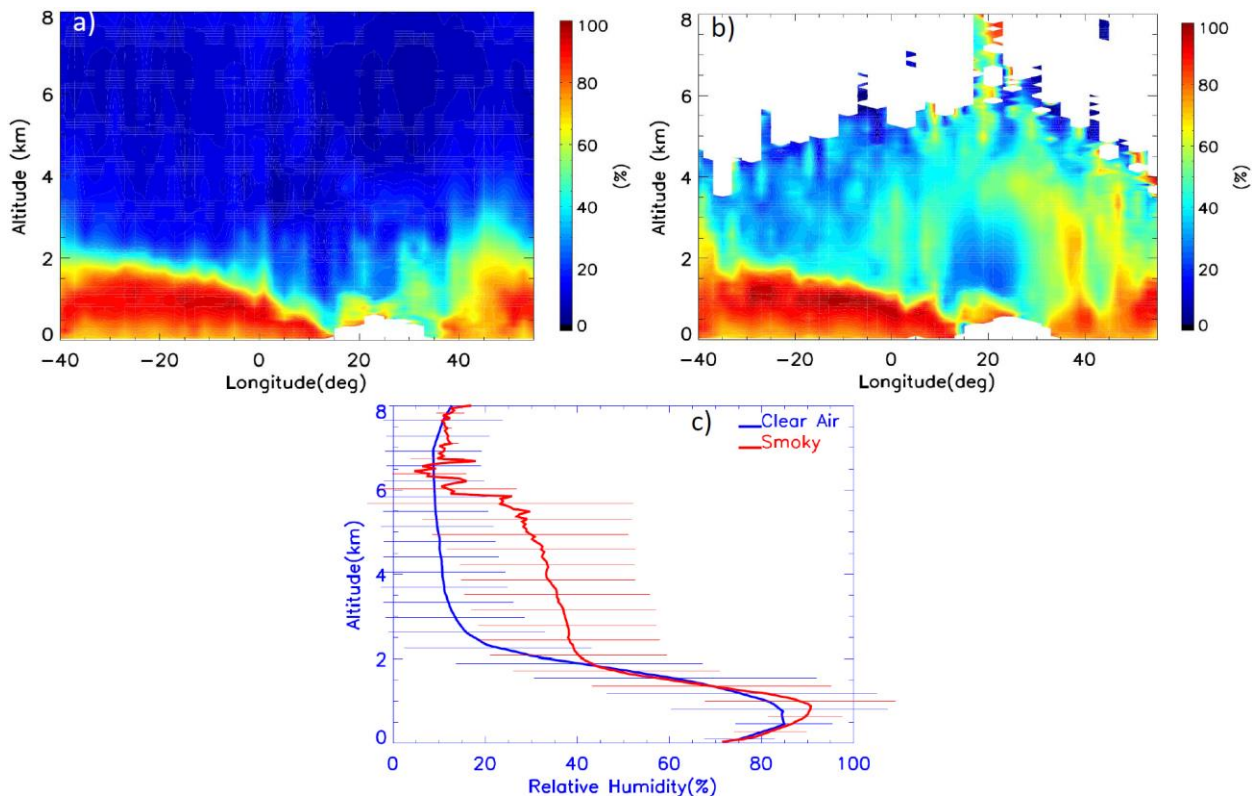
193 retrieved from AVHRR, MODIS, MISR and AERONET through the integration of the GOCART
194 model and the aerosol radiative feedbacks into the atmospheric fields (Randles et al., 2016). The
195 vertical profiles of the total attenuated backscatter from MERRA-2 generally reproduce the
196 CALIPSO vertical profiles at various places over the globe, but show some biases (Randles et al.,
197 2016). Insofar as MERRA-2 already incorporates aerosol information, it is important to determine
198 if the results presented above are biased in any way. We found similar particulate color ratio
199 enhancements over the ocean using V3 CALIPSO data, which reported fewer smoke layers but
200 used GEOS-5.7.2 meteorological data that did not assimilate the aerosol information, thus
201 discounting the possibility of any bias coming from the MERRA-2 meteorology. This also implies
202 that the V4 changes in the aerosol subtyping algorithm do not affect our primary result.

203 The increase in size of smoke particles from CALIPSO observations as seen above is
204 consistent with the findings of Sayer et al. (2014), who studied smoke aerosols transported from
205 biomass burning using data from Analysis of Aerosol Robotic Network (AERONET) stations. For
206 African smoke particles reaching Ascension Island (7.98°S, 14.42°W) in the southeast Atlantic
207 Ocean, they found the volume mean radius ($r_{v,f}$) for fine mode particles to be larger by about 0.02
208 μm than at the inland station of Mongu (15.25°S, 23.15°E) in South Africa. This difference is
209 significantly higher than the estimated uncertainty of 0.01 μm for ($r_{v,f}$) (Sayer et al., 2014). They
210 did not find any evidence of data artifacts resulting from calibration or contamination issues and
211 concluded that the larger radius of the smoke particles at Ascension compared to Mongu is likely
212 to be “a real characteristic of the aerosol transported to this area, rather than an artefact”, with
213 aging over the several days of transport over the ocean being one of the possible causes.

214 **3.2 Relative Humidity Variations**

215 We hypothesize that the increase in size of the smoke particles over the ocean may be related to
216 swelling of the particles by water uptake, which might have a signature in the relative humidity
217 (RH) profiles. Figures 4a and 4b show the height longitude distribution of RH from MERRA-2 as
218 available in CALIPSO data files averaged between 25°S and the equator for all August 2006-2010
219 nighttime data. The clear air RH profiles correspond to cloud-free and aerosol-free columns within
220 this area, while the smoky profiles correspond to columns that are cloud-free but contain smoke
221 samples (essentially corresponding to Figure 2b). Enhanced RH values seem to be associated with
222 the biomass burning smoke plumes. As can be seen in Figure 4c, there is a notable difference
223 between the two mean RH profiles between 2 km and 6 km (over the Atlantic ocean, 0-25°S,
224 30°W-10°E) where the RH values for the mean smoky profile are larger than in the clear air mean
225 profile.

226

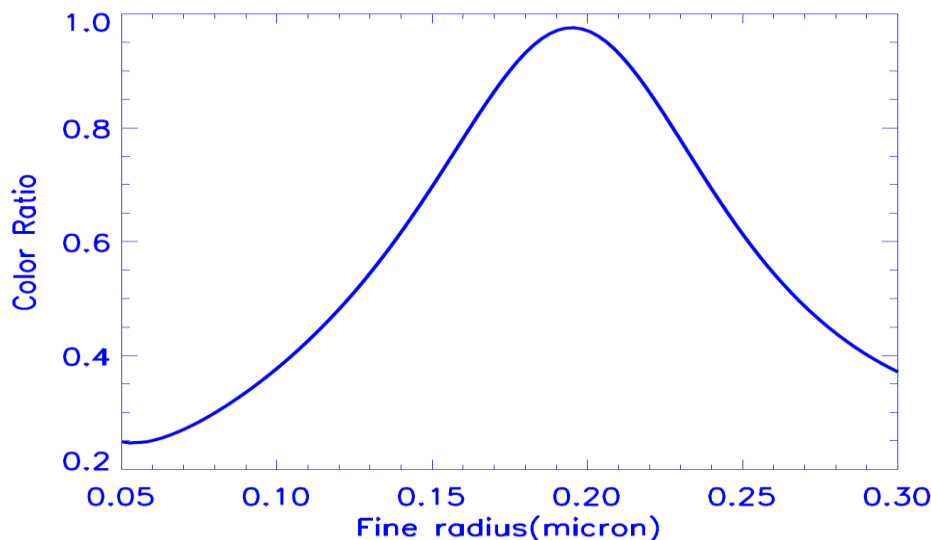


227

228 **Figure 4.** Height-longitude cross sections (0-25°S) of a) relative humidity for clear air
229 profiles, b) relative humidity for profiles with smoke samples in them, and c) averaged
230 profiles and standard deviations of relative humidity over the Atlantic Ocean (0-25°S,
231 30°W-10°E), using all data for August, 2006-2010.

232 Adebisi et al. (2015) had earlier shown that the RH profiles from MERRA on average tend to
233 reproduce the large scale features from high resolution radiosonde profiles obtained at St. Helena
234 Island (~16°S, 6°W), which is located near the southern parts of this study region. The deviation
235 in the mean RH profiles between MERRA and radiosondes is ~10% (Adebisi et al., 2015).
236 However the bias changes sign around 700 hPa. Below this pressure level, MERRA profiles have
237 a low bias as compared to sondes; above this pressure level, they have a higher bias. Note,
238 however, that Adebisi et al. (2015) used an earlier version of the MERRA product, and not the
239 MERRA-2 reanalyses.

240 The mid-tropospheric difference between the smoky and the clear air RH profiles in Figure
241 4c is quite similar to the results of Adebisi et al. (2015) at St. Helena Island, representing the
242 difference between polluted and non-polluted conditions in September-October. Adebisi et al.
243 (2015) presented individual CALIPSO smoke extinction profiles which often closely matched that
244 of the radiosonde RH profiles at St. Helena with high RH values (~ 80%) at the top of the smoke
245 layer with the largest extinction coefficients. In contrast, the RH profiles for the non-smoke days
246 showed much lower RH values ($\leq 20\%$) in the mid troposphere. Adebisi et al. (2015) did not
247 discuss the possible swelling effects on the smoke particles, though they did mention the possibility
248 of this occurring. The increase in moisture collocated with increased aerosol loading suggests an
249 environment conducive for swelling of smoke particles. The increase in particulate color ratio of
250 the smoke particles suggesting increased size is thus quite consistent with this scenario.



252

253 **Figure 5.** Change in the color ratio with volume mean fine radius of smoke particles.

254 The refractive indices of $1.5170 - 0.0234i$ at 532 nm and $1.541 - 0.0298i$ at 1064 nm are

255 consistent with the smoke model in Omar et al., 2009.

256 In Figure 5 we investigate the changes in color ratio as a function of volume mean fine radius using

257 Mie scattering models. The inputs of the fixed parameters are from the fine mode of CALIPSO

258 smoke parameters in Table 1 of Omar et al. [2009]. Further, we have used a fine mode fraction of

259 0.99 for this calculation. Figure 5 shows a near linear relationship between the color ratio and the

260 mean radius when the radius is between typical values of 0.10 – 0.18 for smoke aerosols. In this

261 range, a color ratio change of 0.2 (consistent with the land to ocean difference in particulate color

262 ratio as seen in Fig. 2) corresponds to a mean radius change of $0.03 \mu\text{m}$ which is somewhat larger

263 than the $0.02 \mu\text{m}$ difference reported by Sayer et al. (2014). The color ratio plot is only a first-

264 order approximation of the changes in optical properties of a swelling particle, since the effects of

265 adding water (refractive index of $1.33 - 0i$ at 20°C) to the smoke particle are not accounted for in

266 this example. A more realistic modelling will need to consider co-variation of the complex

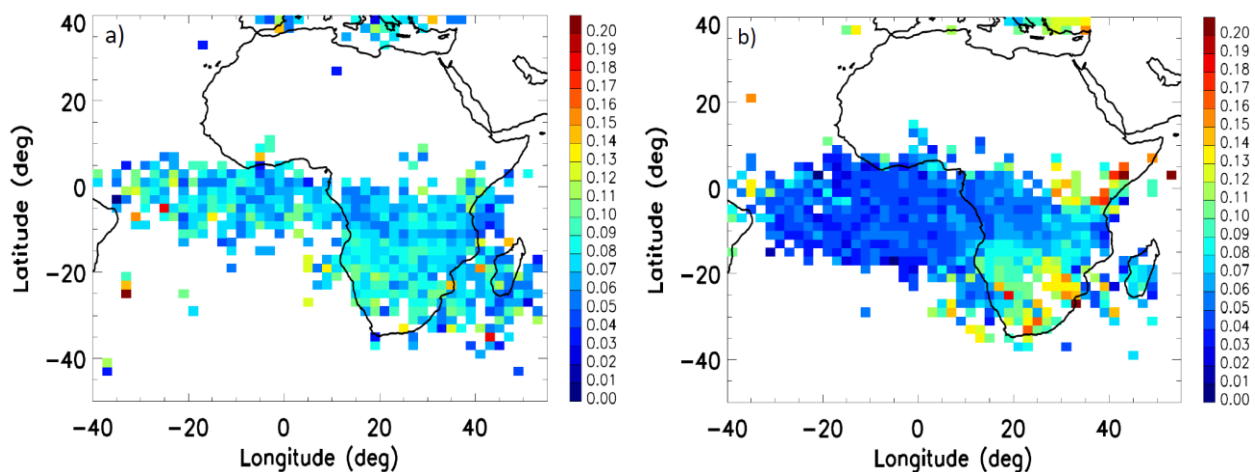
267 refractive indices at both wavelengths, aging as well as the mixing state, and is beyond the scope
268 of the present study.

269

270 3.3. Particulate depolarization of smoke

271 The particulate depolarization ratio (i.e., the ratio of the backscatter in the perpendicular and
272 parallel channels at 532 nm) reported in the CALIPSO data provides insight into the shape of the
273 scattering particles. The particulate depolarization ratio values for the various aerosol subtypes
274 range between 0 and ~0.5, with a mean value of about 0.04-0.05 for smoke and polluted continental
275 to 0.27 for dust (Liu et al., 2015). Polluted dust has a mean value of about 0.13 and marine near
276 0.02 and dusty marine about 0.15. The values of the estimated uncertainties for the various
277 subtypes peak in the range of 200%-300%. In general, swelling might be expected to enhance the
278 sphericity of particles. However, because biomass burning typically generates quasi-spherical
279 particles having low depolarization ratios (Burton et al., 2013), it may be difficult to detect further
280 changes in particle shape using this measurement.

281



283 **Figure 6.** a) Particulate depolarization of smoke at 532 nm at 3 km from CALIPSO for
284 August, 2006-2010 and b) volume depolarization of smoke at 1064 nm at 3 km from CATS
285 for August 2015-2016. A minimum number of 15 samples per grid box was used for each
286 plot. Only nighttime data were used from both instruments.

287 Figure 6a shows the spatial distribution of the particular depolarization (532 nm) of smoke samples
288 at 3 km from CALIPSO, once again using only nighttime cloud free profiles in August for 2006-
289 2010. We rejected depolarization data having estimated relative uncertainty above 500%. This
290 criterion removes data points with very low negative particulate depolarization with associated
291 uncertainties much higher than 500%. There is significant noise in the data with only a suggestion
292 of a somewhat higher depolarization over the land areas over South Africa as compared to the
293 oceanic regions. As an independent measurement, Figure 6b shows the spatial distribution of the
294 volume depolarization of smoke at 3 km at 1064 nm as observed by the CATS lidar for August
295 2015-2016. The CATS data products do not report particulate depolarization ratios. However,
296 because molecular contributions to the backscatter signal at 1064 nm are substantially smaller than
297 at 532 nm (by a factor of ~ 17), the CATS 1064 nm volume depolarization ratios should provide
298 essentially the same information as the particulate depolarization ratios. The effect of swelling is
299 seen a bit more clearly in the CATS 1064 nm depolarization ratio data, with somewhat higher
300 values over the source regions in southern Africa and falling off over the Atlantic Ocean. The
301 significantly higher depolarization of smoke particles south of 18°S may be related to aging of the
302 particles in the anticyclonic gyre over this region (Figure 2a). In general the burning over Southern
303 Africa takes place in dry conditions and produces soot particles which tend to be non-spherical as
304 compared to the wet burning near the equator (Midzak et al., 2017). Note that CATS data products
305 are only available at 1064 nm, so we cannot confirm the changing color ratio using the CATS data.

306 **4. Discussion and Conclusions:**

307 We have presented evidence of a possible increase in the size of smoke particles that are
308 transported over the South Atlantic Ocean in large amounts from the biomass burning regions of
309 South Africa, as reflected in the particulate color ratios retrieved from the CALIPSO space borne
310 lidar. While we have presented the results for the month of August, the same color ratio
311 enhancements in smoke plumes were observed from June through October. The enhanced RH
312 profiles for smoke samples in the mid troposphere as compared to the clear air samples suggests
313 an association with water uptake by these particles. As such, there have been reports of
314 significantly increased moisture content in biomass burning smoke plumes, particularly for
315 smoldering fires (Achtemeir, 2006, Clements et al., 2006). In Southern Africa, smoldering fires
316 may be more frequent towards the equator during the wet season (Midzak et al., 2017). A number
317 of studies have confirmed the hygroscopicity of smoke under certain conditions. Semeniuk et al.
318 (2007) studied the hygroscopic behavior of 80 aerosol particles sampled from southern African
319 burning sources during the SAFARI 2000 mission, which included tar balls and soot, as well as
320 mixed particles. While tar balls and soot were found to be hydrophobic, mixed particles and
321 particles with inorganic coatings showed significantly enhanced hygroscopicity. A similar
322 conclusion about the effect of inorganic material substantially increasing the hygroscopicity of
323 smoke from Siberian fires was also reached by Popovicheva et al. (2016). Further, Vakkari et al.
324 (2014) found that the hygroscopicity of smoke particles, again sampled from South African
325 biomass burning areas, can increase rapidly within the first 2-4 hours due to oxidation and
326 secondary aerosol formation. Aging and further oxidation of the smoke particles as they are
327 transported to vast distances over the ocean may lead to further water uptake. It is possible that
328 there might be other contributing mechanisms apart from swelling. Radke et al. (1995) had made

329 aircraft observations of a large smoke plume that originated in Oregon and was transported over
330 the Pacific Ocean for about 3 days travelling over 1000 km. They found an increase in the size of
331 the accumulation mode particles and argued that coagulation might have been underestimated as
332 a causative mechanism for size changes in smoke plumes. However Radke et al. (1995) did not
333 consider the possible effects of swelling, which seems to be a more likely explanation for our
334 scenario given the correlation with RH as was also observed by Adebisi et al. (2015) over St.
335 Helena. We should mention that beyond the overall difference in RH between the smoke plumes
336 and clear scenes, we did not find a statistically significant linear correlation between the RH
337 enhancements and the color ratio enhancements. This may not be surprising, given the current
338 level of understanding of the hygroscopicity of smoke under different conditions. The relative
339 importance of the composition of smoke particles, the degree of aging as well as the RH level in
340 changing the optical properties of the smoke particles in this area is also not well known at this
341 time.

342 To our knowledge, this is the first report of a change in the size distribution of smoke
343 particles as evidenced from satellite data over this area far from the source regions. The Mie
344 calculations presented here show that the AERONET finding of a significant increase in $r_{v,f}$ at
345 Ascension Island as compared to Mongu (Sayer et al., 2014) is consistent with the color ratio
346 enhancement observed between land to ocean. This is a potentially important result, insofar as the
347 aerosol indirect effect depends strongly on the size of the particles (Spracklen et al., 2011). The
348 enhanced moisture associated with the smoke particles may also be important for radiative forcing
349 and leads to a cooling in September-October in this area (Adebisi et al., 2015). The size increase
350 of smoke particles in this area should also provide important constraints for simulations of this
351 southern African smoke transport, which show significant discrepancies compared to observations

352 (Das et al., 2017). Therefore, this finding needs to be explored further using field missions as well
353 as with satellite data. In fact, a major field mission, ORACLES (Zuidema et al. 2016), is currently
354 studying the aerosol and cloud properties over this very region, and will provide a wealth of
355 resources to validate the results presented here.

356 **5. Acknowledgements:**

357 The CALIPSO aerosol and cloud profile data as well as the CATS lidar data are available at the
358 NASA Langley Research Center Atmospheric Science Data Center. The MERRA 2 wind data
359 were taken from the MERRA-2 Giovanni instance. J. Kar acknowledges useful discussions with
360 Sharon Burton. The authors are grateful to the referees for their useful comments and suggestions
361 which helped improve the paper.

362

363 **References:**

364 Achtemeier, G. L.(2006): Measurements of moisture in smoldering smoke and implications for
365 fog, *Int. J. Wildland Fire*, 15, 517-525.

366
367 Adebisi, A. A. et al. (2015), The convolution of dynamics and moisture with the presence of
368 shortwave absorbing aerosols over the Southeast Atlantic, *J. Clim.*, 28, 1997-2024,
369 doi:10.1175/J-CLI-D-14-00352.1.

370 Bibi, H., K. Alam and S. Bibi, (2016): “In-depth discrimination of aerosol types using multiple
371 clustering techniques over four locations in Indo-Gangetic plains”, *Atmos. Res.*, **181**, 106-
372 114, doi:10.1016/j.atmosres.2016.06.017.

373 Bond, T. C. et al. (2013), Bounding the role of black carbon in the climate system: A scientific
374 assessment, *J. Geophys. Res.*, 118, 5380-5552, doi:10.1002/jgrd.50171.

375 Burton, S. P., et al. (2013), Aerosol Classification from Airborne HSRL and Comparisons with the
376 CALIPSO Vertical Feature Mask. *Atmos. Meas. Tech.*, **6**, 1397-1412.

377 Chand, D. et al. (2008): Quantifying above-cloud aerosol using spaceborne lidar for improved
378 understanding of cloudy-sky direct climate forcing, *J. Geophys. Res.*, **113**, D13206,
379 doi:10.1029/007JD009433.

380 Chand, D., et al. (2009): Satellite-derived direct radiative effect of aerosols dependent on cloud
381 cover, *Nature Geosc.*, **2**, 181-184,doi:10.1038/NGE0437.

382 Clements, C. B., Potter, B. E., and Zhong, S. (2006).: In situ measurements of water vapor, heat,
383 and CO₂ fluxes within a prescribed grass fire, *Int. J. Wildland Fire*, 15, 299-306.

384 Das, S., et al., (2017), Biomass burning aerosol transport and vertical distribution over the South
385 African-Atlantic region, *J. Geophys. Res.*, 122, doi:10.1002/2016JD026421.

386 Deaconu, L. T. et al., (2017): Consistency of aerosols above clouds characterization from A-
387 Train active and passive measurements, *Atmos. Meas. Tech.*, 10, 3499-3523.

388 Getzewich, B. J., et al. (2015): “CALIOP Calibration: Version 4.0 Algorithm Updates”, The 27th
389 International Laser Radar Conference (ILRC 27), *EPJ Web of Conferences*, **119**, 04013,
390 doi:10.1051/epjconf/201611904013.

391 Intergovernmental Panel on Climate Change, IPCC, (2013), *Climate Change 2013: The physical*
392 *science basis. The contribution of working group I to the Fifth Assessment Report of the*
393 *Intergovernmental Panel on Climate Change.*

394 Jethva, H., et al., (2013), A color ratio method for simultaneous retrieval of aerosol and cloud
395 optical thickness of above-cloud absorbing aerosols from passive sensors: Application to
396 MODIS measurements, *IEEE Trans. Geosci. Remote*, 51, 3862-3870,
397 doi:10.1109/TGRS.2012.2230008.

398 Jethva, H et al., (2016), Validating MODIS above-cloud aerosol optical depth retrieved from
399 “color ratio” algorithm using direct measurements made by NASA’s airborne AATS and
400 4STAR sensors, *Atmos. Meas. Tech.*, 9, 5053-5062.

401 Liu, Z., et al. (2009): The CALIPSO Lidar Cloud and Aerosol Discrimination: Version 2
402 Algorithm and Initial Assessment of Performance, *J. Atmos. Oceanic Technol.*, 26,
403 1198–1213, doi:10.1175/2009JTECHA1229.1.

404 Liu, Z., et al., 2015: Evaluation of CALIOP 532-nm AOD over Opaque Water Clouds, *Atmos.*
405 *Chem. Phys.*, 15, 1265–1288, doi:10.5194/acp-15-1265-2015.

406 Meyer, K., S. Platnick and Z. Zhang, (2015), Simultaneously inferring above-cloud absorbing
407 aerosol optical thickness and underlying liquid phase cloud optical and microphysical
408 properties using MODIS, *J. Geophys Res.*, 120, 5524-5547, doi:10.1002/2015JD023128.

409 Midzak, N. et al. (2017), Determining smoke particle sphericity using CATS data, paper
410 presented at the 97th Annual Meeting of the American Meteorological Society, Seattle,
411 Jan 22-27, 2017.

412 Mielonen, T. et al. (2009). Comparison of CALIOP Level 2 aerosol subtypes to aerosol types
413 derived from AERONET inversion data. *Geophys. Res. Lett.*, 36, L18804.

414 Misra, A. K. et al. (2013). Study of MPLNET-derived aerosol climatology over Kanpur, India
415 and validation of CALIPSO Level 2 version 3 backscatter and extinction products.
416 *J. Atmos. Oceanic Technol.*, **29**, 1285–1294.

417 Omar, A. et al. (2009), The CALIPSO automated aerosol classification and lidar ratio selection
418 algorithm, *J. Atmos. Oceanic Technol.*, 26, 1994-2014.

419 Peers, F. et al. (2015), Absorption of aerosols above clouds from POLDER/PARASOL
420 measurements and estimation of their direct radiative effect, *Atmos. Chem. Phys.* 15,
421 4179-4196.

422 Popovicheva, O. B., et al. (2016), Small-scale study of Siberian biomass burning: II. Smoke
423 hygroscopicity *Aerosol and Air Quality Res.*, 16, 1558-1568.

424 Radke, L. F. et al., (1995), Effects of aging on the smoke from a large forest fire, *Atmos. Res*, 38,
425 315-332.

426 Randles, C. A. et al., (2016), The MERRA-2 aerosol assimilation, NASA/TM–2016-104606 /
427 Vol.45, vol. 45, ed. R. D. Koster.

428 Reid, J. S. et al. (2005), A review of biomass burning emissions part III. Intensive optical properties
429 of biomass burning particles, *Atmos. Chem. Phys.*, 5, 827-849.

430 Saide, P. E. (2015): Central American biomass burning smoke can increase tornado severity in
431 the U.S, *Geophys. Res. Lett.*, **42**, 956–965, doi:10.1002/2014GL062826.

432 Sayer, A. M., et al. (2014), AERONET-based models of smoke-dominated aerosol near source
433 regions and transported over oceans, and implications for satellite retrievals of aerosol
434 optical depth, *Atmos. Chem. Phys.*, 14, 11493-11523.

435 Sayer, A. M. et al., (2016), Extending “deep blue” aerosol retrieval coverage to cases of
436 absorbing aerosols above clouds: Sensitivity analysis and first case studies, *J. Geophys.*
437 *Res.*, 121, 4830-4854, doi:10.1002/2015JD024729.

438 Semeniuk, T. A., et al. (2007), Hygroscopic behavior of aerosol particles from biomass fires using
439 environmental transmission electron microscopy, *J. Atmos. Chem.*, 56, 259-273.

440 Spracklen, D. V. et al., (2011), Global cloud condensation nuclei influenced by carbonaceous
441 combustion aerosol, *Atmos. Chem. Phys.*, 11, 9067-9087.

442 Swap, R. J., et al., (2003), Africa burning: A thematic analysis of the Southern African Regional
443 Science Initiative (SAFARI 2000), *J. Geophys. Res.*, 108, 8465,
444 doi:10.1029/2003JD003747.

445 Vakkari, V., et al. (2014), Rapid changes in biomass burning aerosols by atmospheric oxidation,
446 *Geophys. Res. Lett.*, 41, 2644–2651, doi:10.1002/2014GL059396.

447 Van der Werf, G. R., et al. (2010), Global fire emissions and the contribution of deforestation,
448 savanna, forest, agricultural, and peat fires (1997-2009), *Atmos. Chem. Phys.*, 10, 11707-
449 11735.

450 Vaughan, M., et al. (2009): Fully Automated Detection of Cloud and Aerosol Layers in the
451 CALIPSO Lidar Measurements, *J. Atmos. Oceanic Technol.*, 26, 2034–2050, doi:
452 10.1175/2009JTECHA1228.1.

453 Waquet, F. et al., (2013), Retrieval of aerosol microphysical and optical properties above liquid
454 clouds from POLDER/PARASOL polarization measurements, *Atmos. Meas. Tech.*, 6,
455 991-1016,

456 Wilcox, E. M., (2012), Direct and semi-direct radiative forcing of smoke aerosols above clouds,
457 *Atmos. Chem. Phys.*, 12, 139-149.

458 Winker, D. M. et al., (2009), Overview of the CALIPSO mission and CALIOP data processing
459 algorithms, *J. Atmos. Oceanic Technol.*, 26, 2310-2323.

460 Yorks, J. E. et al. (2016), An overview of the CATS Level 1 processing algorithms and data
461 products, *Geophys. Res. Lett.*, 43, 4632–4639, doi:10.1002/2016GL068006.
462 Yu, H. and Z. Zhang, (2013), New directions: Emerging satellite observations of above-cloud
463 aerosols and direct radiative forcing, *Atmos. Environ.*, 72, 36-40.
464 Zuidema, P. et al., (2016): Smoke and Clouds above the Southeast Atlantic: Upcoming Field
465 Campaigns Probe Absorbing Aerosol's Impact on Climate, *BAMS*, 97, 1131–
466 1135,doi:10.1175/BAMS-D-15-00082.1.

467 **List of Figure Captions**

468
469 **Figure 1.** CALIPSO browse images from September 5, 2010 of a) 532 nm attenuated
470 backscatter coefficients; and b) aerosol subtypes reported in the V3 data products;
471 and c) aerosol subtypes reported in the V4 data products.
472 **Figure 2.** a) Particulate color ratio distribution of smoke at 3 km for August, 2006-2010,
473 binned in increments of 2° latitude and 2° longitude, with wind vectors at 700 hPa
474 from MERRA-2 (August 2006-2010) binned in increments of 2.5° latitude and 2.5°
475 longitude; and b) height-longitude cross section of particulate color ratio along 0-
476 25°S (August 2006-2010). Only nighttime data are used.
477 **Figure 3.** Histograms of particulate color ratio over land (25°S-0,10°E-35°E, in blue) and
478 ocean (25°S-0, 30°W-10°E, in aquamarine, filled) at a) 2 km and b) 3 km (August
479 2006-2010).
480 **Figure 4.** Height-longitude cross sections (0-25°S) of a) relative humidity for clear air
481 profiles, b) relative humidity for profiles with smoke samples in them, and c)

482 averaged profiles and standard deviations of relative humidity over the Atlantic
483 Ocean (0-25°S, 30°W-10°E), using all data for August, 2006-2010.

484 **Figure 5.** Change in the color ratio with volume mean fine radius of smoke particles.
485 The refractive indices of $1.5170 - 0.0234i$ at 532 nm and $1.541 - 0.0298i$ at 1064
486 nm are consistent with the smoke model in Omar et al., 2009.

487 **Figure 6.** a) Particulate depolarization of smoke at 532 nm at 3 km from CALIPSO for
488 August, 2006-2010 and b) volume depolarization of smoke at 1064 nm at 3 km
489 from CATS for August 2015-2016. A minimum number of 15 samples per grid
490 box was used for each plot. Only nighttime data were used from both
491 instruments.

492